Large-Area Flexible Core–Shell Graphene/Porous Carbon Woven Fabric Films for Fiber Supercapacitor Electrodes

Xiao Li, Xiaobei Zang, Zhen Li, Xinming Li, Peixu Li, Pengzhan Sun, Xiao Lee, Rujing Zhang, Zhenghong Huang, Kunlin Wang, Dehai Wu, Feiyu Kang, and Hongwei Zhu*

New porous materials are of great importance in many technological applications. Here, the direct synthesis of multi-layer graphene and porous carbon woven composite films by chemical vapor deposition on Ni gauze templates is reported. The composite films integrate the dual advantages of graphene and porous carbon, having not only the excellent electrical properties and flexibility of graphene but also the porous characteristics of amorphous carbon. The multi-layer graphene/porous carbon woven fabric film creates a new platform for a variety of applications, such as fiber supercapacitors. The designed composite film has a capacitance of 20 $\mu F/cm^2$, which is close to the theoretical value and a device areal capacitance of 44 mF/cm^2.

1. Introduction

Carbon is a fascinating material that can be found in various forms, including fullerenes, carbon nanotubes (CNTs), graphene, diamond, and in an amorphous phase. These forms of carbon essentially correspond to different ways of forming a bond between carbon atoms (sp^2 and sp^3). Carbon materials can also form tubes, films, and porous materials, demonstrating the diversity of macrostructures that can be achieved. Different forms of carbon materials have different functions. Graphene, a two-dimensional (2D) form of carbon with atoms arranged in a honeycomb lattice, has received great interest since the discovery of its unique electrical, optical, and other

properties.[1–4] Graphene can be stacked to form graphite or rolled into cylindrical graphene tubes.[5,6] Although many of the properties of multi-layer graphene (MLG) are not better than those of graphene, MLG exhibits unique advantages in conductivity. Moreover, MLG can be more conveniently processed in macroscale applications due to its higher strength.[7,8] Products composed of porous amorphous carbon, a common carbon material, can be highly controlled by changing their synthesis conditions. This allows for a wide range of applications, from selective sorbents to electrical energy storage.[9–11] Hybrid structures of different carbon materials further extend the diversity of carbon-based macrostructures with combined properties inherited from the constituent structures.[12,13] For example, graphene adsorbed on the surface of diamond behaves as a semiconductor with a finite gap, depending on the adsorption parameters, with the added advantage of maintaining the main characteristics of the linear band dispersion of graphene.[14] Composite films made from graphene and CNTs possessed high transparencies and electrical conductivities, showing excellent potential as a transparent electrodes.[15] Solar cells assembled and processed using CNTs and fullerenes represent a new type of all-carbon-composite photovoltaic device.[16]

In this work, we report a new form of carbon-based hybrid structure composed of MLG and porous carbon (PC). The composite films were directly synthesized by chemical vapor deposition (CVD) on Ni gauze templates.[17–19] The MLG/PC core–shell structures were uniform and continuous, with macroscale dimensions on the order of centimeters, which were only limited by the size of the Ni gauze templates. The MLG component was in the form of micrometer-sized tube, which was conformally grown and coated on a Ni wire. The PC component was an amorphous phase distributed throughout the MLG tubes. The characteristics of both MLG and PC have been retained in the hybrid films. By adjusting the formulation and processing conditions, we could control the pore size distribution, density and purity of the carbon. The two-dimensionality, excellent conductivity, porous characteristics, high strength and semi-transparency made the hybrid films ideal materials for many applications. Electrochemical measurements indicated that the N-doped composite film exhibited enhanced capacitive

X. Li, X. B. Zang, Z. Li, X. M. Li, P. X. Li, P. Z. Sun,
X. Lee, R. J. Zhang, Prof. Z. H. Huang,
Prof. K. L. Wang, Prof. D. H. Wu, Prof. F. Y. Kang,
Prof. H. W. Zhu
School of Materials Science and Engineering
Tsinghua University
Beijing 100084, China
E-mail: hongweizhu@tsinghua.edu.cn
Prof. F. Y. Kang
Advanced Materials Institute
Graduate School at Shenzhen
Tsinghua University
Shenzhen 518055, China
X. Lee, Prof. H. W. Zhu
Center for Nano and Micro Mechanics
Tsinghua University
Beijing 100084, China

www.MaterialsViews.com

ADVANCED
FUNCTIONAL
MATERIALS
www.afm-journal.de

FULL PAPER

performance comparing with the pristine film, which was ascribed to the pseudocapacitive effect of the N-doping. The designed composite film had a capacitance of 20 µF/cm² which was close to the theoretical value[20] and a device areal capacitance of 44 mF/cm². Our results suggest that the use of these novel MLG/PC composite films may lead to a new line of portable and wearable nano-devices.

2. Characterizations of MLG/PC Woven Fabric Composites

2.1. Synthesis and Post-Treatment

There have been a number of reports on the CVD growth of graphene on metal substrates, such as Ni, Cu,[21] Pt,[22] Ir,[23] and Ru.[24] Among the various metals investigated, Ni has potential for industrial applications because it is relatively inexpensive and has been proven to be a good CVD substrate. The CVD process occurred at high temperature, and carbon had a significant solubility in Ni. The diffusion of C in Ni was high; therefore, upon cooling, MLG precipitated out. In this work, by tuning methane feeding rates and reaction times, the formation of MLG could be well controlled. The process schematic and resulting MLG/PC woven structures are shown in **Figure 1** (see the Experimental Section for details). The general procedure was to prepare MLG on nickel mesh, etch the nickel wires to form a carbon hybrid of MLG and PC, oxidize the hybrid with acids to produce tree like structure (Figure 1a). By using different types of woven Ni gauzes as templates, MLG/PC of different configurations grown from CVD retained the network structure of the Ni mesh. By tuning the methane feeding rate and reaction time of the CVD process, the graphene layer thickness and PC capacity could be tuned, yielding a wide range of porosity. The MLG/PC film could be easily transferred from one liquid surface to another using glass rollers. Figure 1b shows a typical freestanding sample after being etched for 5 h

in FeCl₃/HCl solution (1 M FeCl₃, 0.5 M HCl). The film could be taken out from the solution, revealing that it is of good structural integrity. This film has a low sheet resistance of less than 10 Ω/sq. Floating the composite film onto concentrated acids (H₂O₂, HNO₃ or H₂SO₄) resulted in dissociation of MLG layers on the PC surface. In comparison to the starting material, the hybrid showed tree-like structure. Figure 1c shows a series of scanning electron microscopy (SEM) images of MLG/PC samples left in acid for differing periods of time. After etching for ≈5–10 min, the graphene leaves were completely lifted up. In nitric and sulfuric acids, the MLG/PC samples could remain stable for days.

2.2. Microstructural Characterizations

As shown in the SEM images (Figure 1c and **Figure 2**a), the MLG/PC film consists of two typical structures. When a small amount of carbon source feed plus a shorter cooling time was employed, the MLG shell thus produced was composed of only a few layers, and most carbon species were concentrated in the PC core. Due to the high flexibility of the MLG shell, the film collapsed on the PC core. When a large amount of carbon source feed as well as a longer cooling time was employed, more carbon species precipitated out from Ni, resulting in thick MLG shells. Even after etching, the MLG was still able to maintain the morphology of the original nickel mesh due to its high strength. If the nickel mesh with the MLG shell on it was polished before the etching process, the PC core could be exposed after etching (Figure 2b,c). The composite film exhibited the characteristics of both the MLG shell and PC core. The thinner walls of MLG would provide a larger specific surface area and voids for high-performance supercapacitor electrodes. The thick walls of MLG would provide a better skeleton structure to be filled with functional materials. The products could be tailored by controlling the reaction conditions. The PC retained the structure of the original solid solution[25] because carbon rearrangement occurred only by diffusion along the nickel/acid interface, and did not involve nucleation of new grains. The MLG leaves and PC structures were observed with the transmission electron microscopy (TEM). Figure 2d,e show high-resolution TEM images in which nanopores are clearly apparent, indicative of the 3D porous network. Selected-area electron diffraction patterns confirmed the entire material is amorphous or polycrystalline.

To further investigate the structural feature of the MLG/PC composite films, the materials were further characterized by Raman spectroscopy.[26,27] The representative Raman spectra of graphene and PC are presented in Figure 2f. The MLG spectrum shows the characteristics of the typical multilayer graphite. Two Raman scattering bands are clearly observed. The peak at 1580 cm⁻¹ (G band) corresponds to crystalline sp² hybridization and the broad peak at 2725 cm⁻¹ (2D band) is the typical peak for
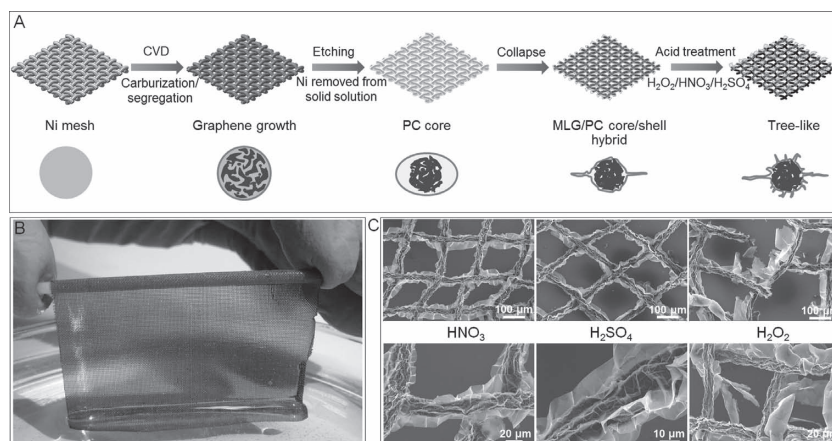

Figure 1. Fabricating MLG/PC woven fabrics using nickel wire meshes as substrates. A) Schematic of steps for MLG/PC preparation. Bottom plane shows corresponding cross-sectional views of a core–shell structure. B) Optical image of a 10-cm wide MLG/PC film. C) SEM images of MLG/PC woven fabrics treated by acids.
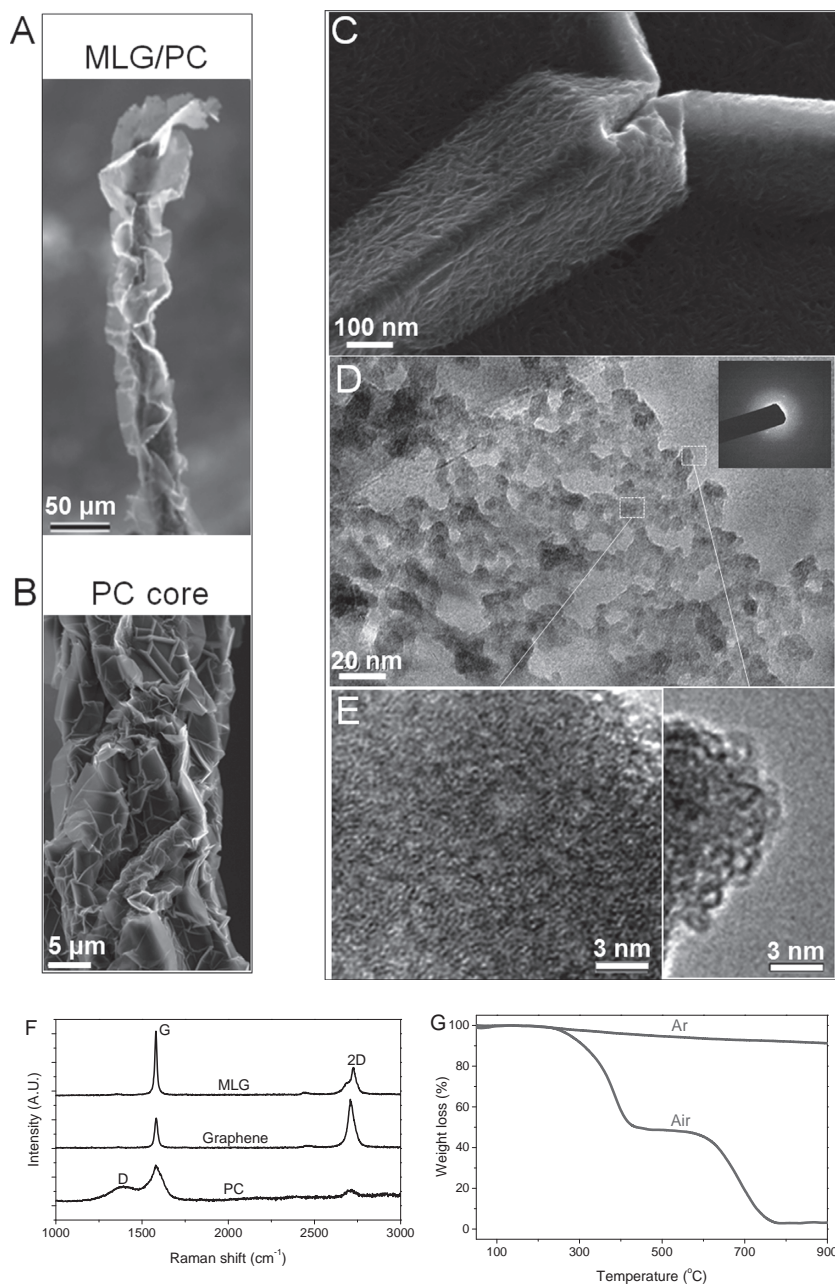
ADVANCED
FUNCTIONAL
MATERIALS
www.afm-journal.de

Materials
Views
www.MaterialsViews.com

FULL PAPER

Figure 2. Microstructural characterizations of the MLG/PC core–shell composites. A–E) SEM and TEM images, showing the hierarchal pore structure. Inset of (C) shows the electron diffraction pattern of the PC core. F) Raman spectra of graphene and PC. G) TGA profiles of the composite film tested in air and argon.

crystalline graphite, suggest that the PC core is composed mainly of an amorphous phase and graphite particles.

X-ray diffraction (XRD) analysis is a fundamental technique for studying carbon stacking structures.[28,29] The crystallinity and structure of the composite films were analyzed by XRD, and the corresponding diffraction profiles for the MLG shell and PC core are shown in Figure S1 (Supporting Information). Both of them have a dominant sharp peak at 26.6° (MLG) and 26.2° (PC), corresponding to the (002) plane of graphite. The (002) peak for the PC core is dramatically broadened and shows a remarkably reduced intensity. These results confirm that the MLG shell is composed of predominantly layered carbon, and the PC core contains a significant amount of highly disordered material, amorphous carbon, which is also responsible for the background intensity of the diffraction. The strong decrease in the (002) peak is clear and an apparent increase in the peak band is also noted, which is consistent with the presence of a high density of pores. These results are in good agreement with the observations made by TEM.

Figure 2g shows the results of thermogravimetric analysis (TGA) under an ambient and an argon atmosphere.[30] The results obtained in air clearly show two weight-loss processes due to the different heat resistances of the MLG shell and PC core. The first pronounced weight loss at between ≈250–450 °C is associated with the PC core, corresponding to a weight loss of ≈50–70%. The next step, in the range of ≈600–750 °C, is due to the oxidization of the MLG shell. The composite film shows good thermal stability in argon. The TGA results show that the as-prepared composite film experiences a weight loss of less than 10% at temperatures up to 900 °C in argon. Furthermore, after high-temperature treatment, the composite film is still able to maintain a good three-dimensional structure, which is advantageous for use as a support structure for material filling.

graphite. There is no obvious D band, implying highly crystalline structure of the MLG shell. Similarly, three Raman scattering bands are observed in the PC core. The peak at approximately 1379 cm^{-1} (D band) is considered to represent a disordered structure and is commonly present in the range of 1297–1479 cm^{-1}. The intensity of the D band characterizes the PC core's degree of deviation from perfect symmetry. Moreover, the G band at 1580 cm^{-1} and the second-order overtone of the D band, i.e., the broad 2D band (2711 cm^{-1}), corresponding to

2.3. Porous Structure Evaluation

SEM images of the PC core are shown in **Figure 3**a–c to provide further information regarding the core's porous structure. As the etching process proceeded, the carbon species in solid solution were slowly separated out from Ni and formed a PC core with many folds on the surface. The inside and outside of the PC core were rich in nanoscale holes. The nitrogen adsorption/desorption isotherms of the as-prepared composite
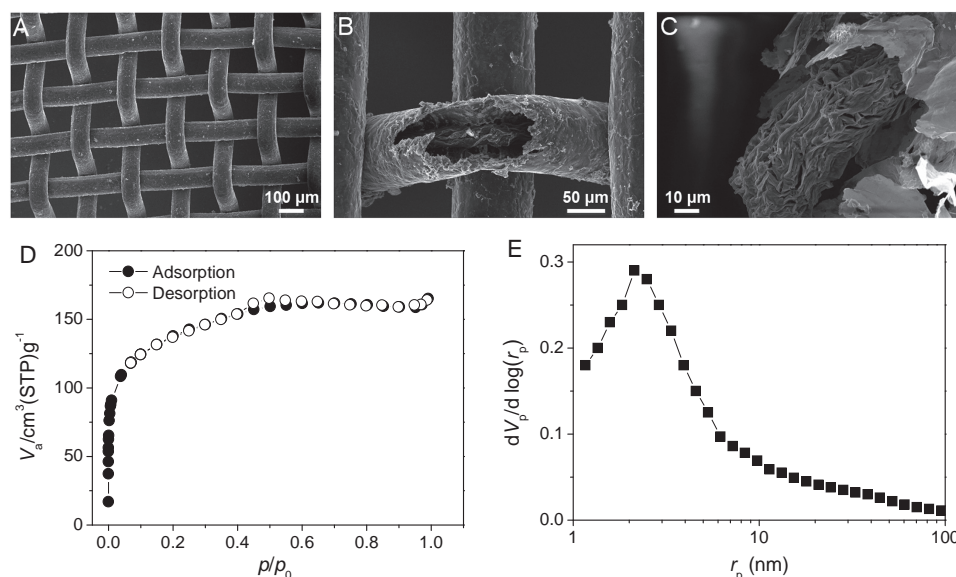
www.MaterialsViews.com

ADVANCED
FUNCTIONAL
MATERIALS
www.afm-journal.de

FULL PAPER

Figure 3. A–C) SEM images showing the MLG layers and PC cores. D) Nitrogen adsorption/desorption isotherms and E) corresponding pore-size distribution of a typical MLG/PC sample.

film (Figure 3d) shows a typical type-I isotherm. It is clear that the degree of adsorption increases rapidly at low relative pressure in the adsorption line, implying the existence of a large amount of micropores. As the relative pressure increases, the adsorption capacity of the sample continues to increase, suggesting the presence of mesopores in the sample. The adsorption isotherms and desorption isotherms do not completely overlap. The hysteresis loop between the adsorption and desorption branches implies the existence of a small amount of macropores. The specific surface area of the samples was measured to be ≈688 m^2/g, with a total pore volume of 435 m^3/g. In addition, the pore size distribution of the sample reveals that the pore size is mainly in the mesoporous range and the mean pore size of the sample is in the range of ≈2–3 nm (Figure 3e). Considering the fact that the effective radii of most salt ions are in the range of ≈0.5–1.5 nm, the average pore size of the composite film favors the formation of an electrical double-layer of target ions.[31]

2.4. Nitrogen Doping

Many previous studies have used nitrogen as a dopant and/or nitrogen-containing functional groups to enhance the device performance of graphene, especially in supercapacitors.[32–34] The doping process and the preparation process were performed at the same time. As methane (20 mL/min) was introduced into the quartz tube as the carbon source, ammonia (5 mL/min) was added as the nitrogen source. **Figure 4**a,b show the SEM images of the MLG shell and PC core after the preparation and etching process. Due to the introduction of nitrogen, the formation of the MLG shell was restrained and many holes appeared. In addition, the morphology of the PC core was also affected, showing more defects and grooves. The nitrogen bonding configurations are further discussed

based on the XPS results (Figure 4c). The XPS profile shows the presence of carbon, nitrogen, and oxygen atoms. For the composite film, the C1s spectrum indicates large amounts of sp^3 carbon with C-O or C-N bonds, which results from the destruction of the sp^2 atomic structure of graphite. Moreover, the O (17.8%) and N (2.5%) content suggest the same result. By doping, nitrogen atoms are expected to replace carbon atoms in graphene sheets and form three types of C/N structures. In this work, the bonding configurations of nitrogen atoms were confirmed by high-resolution XPS, and the results show two main peaks. The peak at 398.2 eV is ascribed to pyridine N structures (N6 in Figure 4d), contributing to the π-conjugated system with a pair of p-electrons in graphene layers. The peak at 399.8 eV is attributed to pyrrole N structures (N5 in Figure 4d), which are associated with N-doping in the form of –NH. The sample exhibits excellent N-doped thermal stability. It is also expected that the N-doping process would significantly improve the electrochemical performance.

2.5. Supercapacitor Electrodes

The composite films were used to assemble supercapacitors in a simple way.[35–37] First, the films were first twined on metal wire electrodes (e.g., platinum) (**Figure 5**). Then, the dry samples were placed in a quartz tube furnace with argon flowing from 30 to 800 °C for 2.5 h and at 800 °C for 1 h. The performance of the MLG/PC-based supercapacitors was measured in an electrochemical system. The film was directly adhered to a platinum wire and used as the fiber electrode for supercapacitors operated in a 1 mol/L aqueous Na_2SO_4 electrolyte. The electrochemical performances of the N-doped films (≈35–100 μm diameter with different configurations, see Figure 5b–d) were examined using the cyclic voltammetry (CV) method. **Figure 6**a,b show

ADVANCED
FUNCTIONAL
MATERIALS

www.afm-journal.de
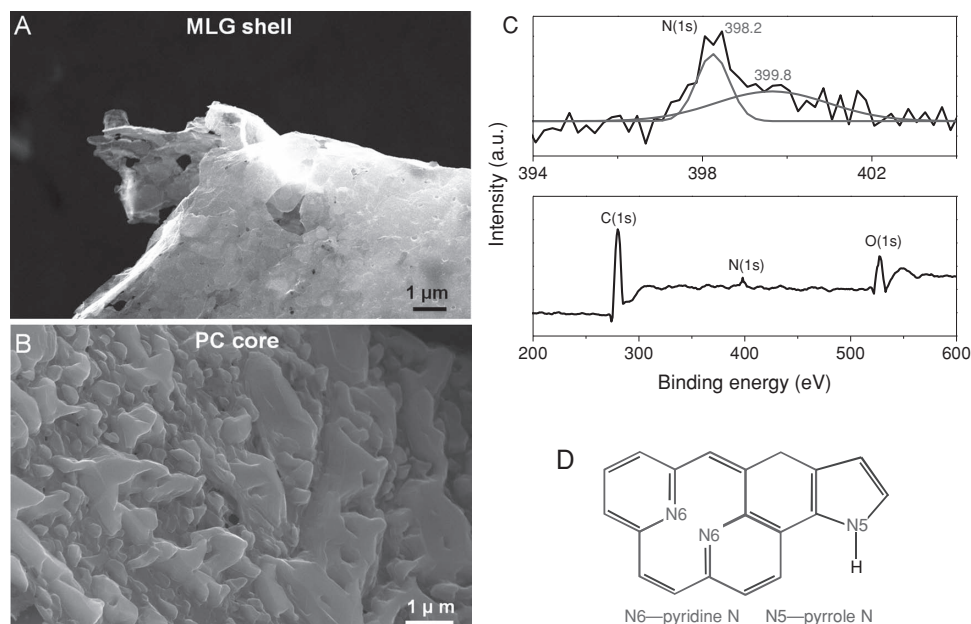
Materials Views
www.MaterialsViews.com

Figure 4. N-doping of the MLG/PC composite. SEM images of N-doped A) MLG and B) PC. C) XPS spectra. D) Molecular model of N-doping of graphene.

a set of CV curves with scan rate from 10 to 500 mV/s within a 0.0–0.7 V voltage window. These curves show a nearly ideal rectangular shape when the rate is less than 200 mV/s, indicating that the device has excellent supercapacitor behavior even at high area density. The supercapacitor based on the nitrogen-doped MLG/PC film shows a capacitance of 173 F/g (Figure 6c) (225 F/g for MnO_2 coated electrodes), which is about 1.5 times higher than the capacitance of pristine MLG/PC-film-based counterparts, without sacrificing other essential and useful properties for supercapacitor operations, including high power capability, excellent cycle life and compatibility with flexible substrates.

The diameter of the nickel wire is an important factor influencing the supercapacitor performance. Supporting Information Figure S2 shows the rate-dependent normalized capacitances of supercapacitors made from nickel wires of different

diameters. N-doped, small-diameter wires are preferred for supercapacitor applications, with the capacitance reaching 23.4 $\mu F/cm^2$ for N-doped, 35-μm thick wires. The rate capability of the supercapacitor was also enhanced by N-doping with small-diameter wires, showing only a ≈20% capacitance loss (20.5 to 16.4 $\mu F/cm^2$) when the scan rate was increased from 10 to 500 mV/s, which is much better compared to the sample featuring a pristine film and 100-μm-thick wires (86% capacitance loss, 5.83 to 0.72 $\mu F/cm^2$).

Table 1 summarizes the specific capacitance (SC) values of the MLG/PC based supercapacitor. The specific device-area capacitance (SC_{DA}) is the most important parameter for large-area application, because of the limited space available. Though the gravimetric capacitance of the MLG/PC based device is moderate, considering its high SC_{DA} value (44.7 mF/cm²), the composite film combining the special woven structure and high flexibility and semi-transparency still represents a potentially promising candidate for large-area energy-related applications.[38,39]

The voltage versus time profiles obtained by the galvanostatic charge-discharge technique conducted at different currents (inset of Figure 6d) show highly linear behavior and a nearly symmetrical shape, which also confirm the ideal capacitive behavior. The capacitance reached 173 F/g at 20 A/g. The film showed a 5% capacitance loss after 1000 cycles at 20 A/g, revealing its good electrochemical stability.

Figure 6e shows the electrochemical impedance spectra of the N-doped composite film in 1 mol/L Na_2SO_4 with an amplitude of 0.02 V. The plot shows a vertical curve, indicating the good capacitive behavior of
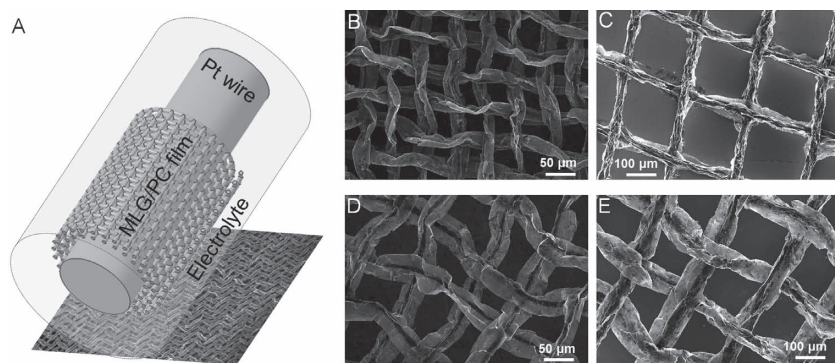

Figure 5. A) Schematic of a MLG/PC fiber electrode of the supercapacitor. SEM images of MLG/PC woven fabrics of four different configurations: B) W = 35 μm, 400 mesh; C) W = 50 μm, 20 mesh; D) W = 50 μm, 200 mesh; E) W = 100 μm, 100 mesh. W represents the diameter of the Ni wire.

www.MaterialsViews.com

ADVANCED
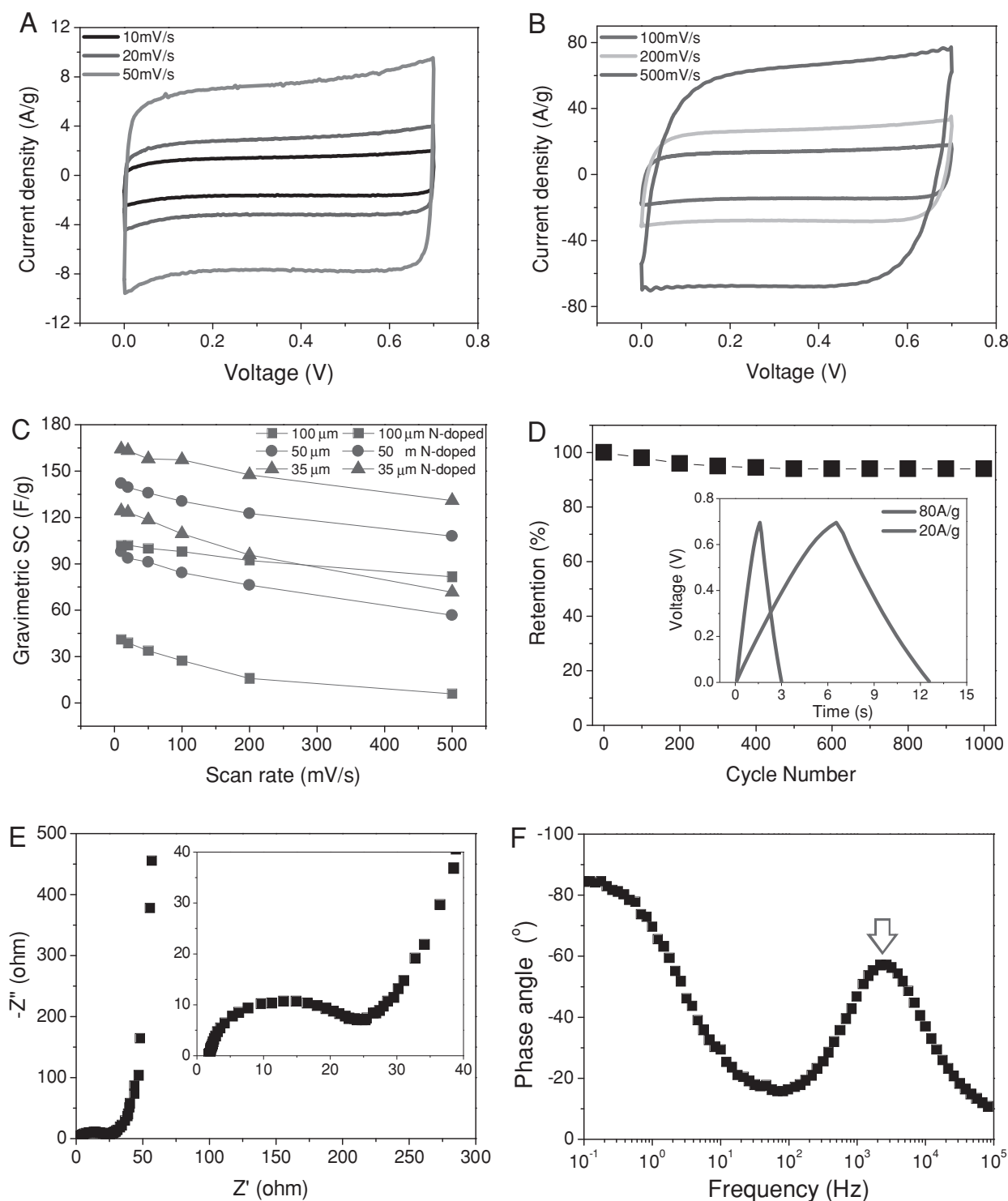FUNCTIONAL
MATERIALS
www.afm-journal.de

FULL PAPER

Figure 6. Electrochemical performance of MLG/PC based supercapacitors. A,B) CV curves for different scan rates. Rectangular shapes indicate the capacitive behavior. C) Relationship between the gravimetric specific capacitance and the scan rate. D) Cycling behavior and galvanostatic charge–discharge curves under different constant currents (inset). E) Nyquist plot showing the imaginary part versus the real part of impedance. Inset shows the enlarged view of the low impedance range. F) Frequency response of the phase angle.

the device. However, the presence of a high-frequency semi-circle was caused by the charge transfer resistance,[40] implying the ionic conductivity at the interface of the electrodes and

electrolyte could be further optimized. The equivalent series resistance obtained from the X-intercept of the Nyquist plot (inset of Figure 6e) is about ≈23 Ω. The impedance phase angle

Table 1. The specific capacitance (*SC*) values of the MLG/PC based supercapacitor.

Gravimetric SC [F/g]		Surface areal SC [μF/cm^2]	Device areal SC [mF/cm^2]	Pore volumetric SC [mF/m^3]
$SC_G = \frac{1}{s \cdot m \cdot \Delta V} \int_{V_0}^{V_0 + \Delta V} I\, dV$ [a)]		$SC_{SA} = \frac{C_G}{S_a}$ [b)]	$SC_{DA} = \frac{C_G \cdot m}{S_d}$ [c)]	$SC_{PV} = \frac{C_G}{V_p}$ [d)]
173		20.5	44.7	328

[a)]*I* - Current, *s* - Scan rate, *m* - Sample mass; [b)]S_a - Specific surface area; [c)]S_d - Device area; [d)]V_p - Pore volume.

plot is shown in Figure 6f from 100 KHz to 0.1 Hz. Most supercapacitors show a similar capacitor-to-inductor transition at AC frequencies as the frequency increases. The nearly −90° phase angle at low frequencies indicates capacitive behavior. Although the capacitor-to-inductor transition occurred as the frequency increased, the capacitor device showed a stronger response between 10^2 and 10^4 Hz. The supercapacitors were observed to always retain their capacitance characteristics.

Compared to their counterparts, our supercapacitors integrate the electrical conductivity of graphene and the porous characteristics of amorphous carbon. Most importantly, the capacitor electrodes were directly fabricated by CVD. Due to the unique skeleton structure, these films could also be used as support structures for functional materials filling to further improve the capacity performance (e.g., MnO_2 filling)[41,42] or make the composite film magnetic (e.g., Fe_3O_4 filling),[43] as shown in Supporting Information Figure S3. For example, MnO_2 nanoparticles were deposited on the surfaces of the MLG and PC by a facile and effective chemical method (see the Supporting Information), which improved the capacitor performance by 30% to 225 F/g.

3. Conclusions

In summary, we report the direct synthesis of multi-layer graphene and porous carbon (MLG/PC) woven composite films by chemical vapor deposition on Ni gauze templates. The composite films integrated the dual advantages of graphene and PC, having not only the excellent electrical properties and flexibility of graphene but also the porous characteristics of amorphous carbon. The MLG/PC woven fabric film created a new platform for a variety of applications, such as supercapacitor electrode materials. By carefully tuning the synthesis parameters and nitrogen doping, the specific capacitances of the supercapacitors based on the composite films reached 44 mF/cm^2 (device areal) and 20 μF/cm^2 (surface areal), illustrating the promise for use as electrodes for portable and wearable energy storage.

4. Experimental Section

Synthesis of MLG/PC Woven Fabric Composite Films: A Ni gauze template (wire diameter: ≈35–100 μm, ≈20–400 mesh) was first prepared by cleaning with hydrochloric acid and water as shown in Figure 1a. After argon drying, the Ni gauze template was placed in the middle of a quartz tube located in a CVD thermal furnace. When the furnace was heated to 1000 °C, ethanol was introduced at 20 mL/min into the quartz tube as the carbon source. After a 20 min reaction, the

sample was cooled to room temperature under argon flow. The as-obtained MLG/PC film is shown in Figure 1b. After etching Ni away using a $FeCl_3$/HCl solution ($FeCl_3$: 1 mol/L, HCl: 0.5 mol/L), solid dissolved carbon separated out into the amorphous form along the axis of the MLG microtube.

Electrochemical Test: To prepare the electrode for the fiber supercapacitor, the platinum wire was wrapped up with the MPG/PC fabric film. The electrochemical data were recorded with a CHI 660B electrochemical workstation (Shanghai CH Instrument Co.) at a scan rate of 10–500 mV/s within the potential range of 0.0–0.7 V.

Supporting Information

Acknowledgements

[1] K. S. Novoselov, A. K. Geim, S. V. Morozov, D. Jiang, Y. Zhang, S. V. Dubonos, I. V. Grigorieva, A. A. Firsov, *Science* **2004**, *306*, 666.

[2] F. Schedin, A. K. Geim, S. V. Morozov, E. W. Hill, P. Blake, M. I. Katsnelson, K. S. Novoselov, *Nat. Mater.* **2007**, *6*, 652.

[3] D. A. Areshkin, C. T. White, *Nano Lett.* **2007**, *7*, 3253.

[4] X. L. Li, X. R. Wang, L. Zhang, S. W. Lee, H. J. Dai, *Science* **2008**, *319*, 1229.

[5] R. Wang, Y. F. Hao, Z. Q. Wang, H. Gong, J. Thong, *Nano Lett.* **2010**, *10*, 4844.

[6] L. J. Zhi, T. Gorelik, J. S. Wu, U. Kolb, K. Mullen, *J. Am. Chem. Soc.* **2005**, *127*, 12792.

[7] X. Li, P. Z. Sun, L. L. Fan, M. Zhu, K. L. Wang, M. L. Zhong, J. Q. Wei, D. H. Wu, Y. Cheng, H. W. Zhu, *Sci. Rep.* **2012**, *2*, 395.

[8] A. Reina, X. T. Jia, J. Ho, D. Nezich, H. B. Son, V. Bulovic, M. S. Dresselhaus, J. Kong, *Nano Lett.* **2009**, *9*, 3087.

[9] D. Hulicova-Jurcakova, M. Seredych, Y. G. Jin, G. Q. Lu, T. J. Bandosz, *Carbon* **2010**, *48*, 1767.

[10] V. Presser, M. Heon, Y. Gogotsi, *Adv. Funct. Mater.* **2011**, *21*, 810.

[11] P. Gonzalez-Garcia, T. A. Centeno, E. Urones-Garrote, D. Avila-Brande, L. C. Otero-Diaz, *Mater. Chem. Phys.* **2011**, *130*, 243.

[12] D. S. Yu, L. M. Dai, *J. Phys. Chem. Lett.* **2010**, *1*, 467–470.

[13] D. Yu, K. Park, M. Durstock, L. M. Dai, *J. Phys. Chem. Lett.* **2011**, *2*, 1113.

[14] Y. D. Ma, Y. Dai, M. Guo, B. B. Huang, *Phys. Rev. B* **2012**, *85*.

[15] C. Y. Li, Z. Li, H. W. Zhu, K. L. Wang, J. Q. Wei, X. A. Li, P. Z. Sun, H. Zhang, D. H. Wu, *J. Phys. Chem. C* **2010**, *114*, 14008.

[16] V. C. Tung, J. H. Huang, J. Kim, A. J. Smith, C. W. Chu, J. X. Huang, *Energy Environ. Sci* **2012**, *5*, 7810.

[17] H. J. Park, J. Meyer, S. Roth, V. Skakalova, *Carbon* **2010**, *48*, 1088.

[18] K. S. Kim, Y. Zhao, H. Jang, *Nature* **2009**, *457*, 706.

[19] Z. P. Chen, W. C. Ren, L. B. Gao, B. L. Liu, S. F. Pei, H. M. Cheng, *Nat. Mater.* **2011**, *10*, 424.

Materials
Views

www.MaterialsViews.com

ADVANCED
FUNCTIONAL
MATERIALS

www.afm-journal.de

FULL PAPER

[20] H. Shi, *Electrochim. Acta* **1996**, *41*, 1633.

[21] X. S. Li, W. W. Cai, J. H. An, S. Kim, H. Nah, D. X. Yang, R. Piner, A. Velamakanni, I. Jung, E. Tutuc, S. K. Banerjee, L. Colombo, R. S. Ruoff, *Science* **2009**, *324*, 1312.

[22] P. Sutter, J. T. Sadowski, E. Sutter, *Phys. Rev. B* **2009**, *80*.

[23] J. Coraux, A. T. N'Diaye, C. Busse, T. Michely, *Nano Lett.* **2008**, *8*, 565.

[24] K. F. McCarty, P. J. Feibelman, E. Loginova, N. C. Bartelt, *Carbon* **2009**, *47*, 1806.

[25] R. B. Mclellan, P. Chraska, *Mater. Sci. Eng.* **1970**, *6*, 176.

[26] M. S. Dresselhaus, A. Jorio, M. Hofmann, G. Dresselhaus, R. Saito, *Nano Lett.* **2010**, *10*, 751.

[27] A. N. Obraztsov, A. V. Tyurnina, E. A. Obraztsova, A. A. Zolotukhin, B. H. Liu, K. C. Chin, A. Wee, *Carbon* **2008**, *46*, 963.

[28] Y. S. Dedkov, M. Sicot, M. Fonin, *J. Appl. Phys.* **2010**, *107*.

[29] B. Manoj, A. G. Kunjomana, *Int. J. Electrochem. Sci.* **2012**, *7*, 3127.

[30] S. T. Senthilkumar, B. Senthilkumar, S. Balaji, C. Sanjeeviraja, R. K. Selvan, *Mater. Res. Bull.* **2011**, *46*, 1320.

[31] X. Li, J. Rong, B. Q. Wei, *ACS Nano* **2010**, *4*, 6039.

[32] L. L. Zhang, X. Zhao, H. X. Ji, *Energy Environ. Sci.* **2012**, *5*, 9618.

[33] H. M. Jeong, J. W. Lee, W. H. Shin, Y. J. Choi, H. J. Shin, J. K. Kang, J. W. Choi, *Nano Lett.* **2011**, *11*, 2472.

[34] L. F. Chen, X. D. Zhang, H. W. Liang, M. G. Kong, Q. F. Guan, P. Chen, Z. Y. Wu, S. H. Yu, *ACS Nano* **2012**, *6*, 7092.

[35] K. Xie, X. T. Qin, X. Z. Wang, Y. N. Wang, H. S. Tao, Q. Wu, L. J. Yang, Z. Hu, *Adv. Mater.* **2012**, *24*, 347.

[36] Y. W. Zhu, S. Murali, M. D. Stoller, *Science* **2011**, *332*, 1537.

[37] F. Liu, S. Y. Song, D. F. Xue, H. J. Zhang, *Adv. Mater.* **2012**, *24*, 1089.

[38] X. Li, T. L. Gu, B. Q. Wei, *Nano Lett.* **2012**, *12*, 6366.

[39] Y. P. Fu, X. Cai, H. W. Wu, Z. B. Lv, S. C. Hou, M. Peng, X. Yu, D. C. Zou, *Adv. Mater.* **2012**, *24*, 5713.

[40] V. Subramanian, H. W. Zhu, C. Masarapu, K. H. Hung, Z. Liu, K. Suenaga, B. Q. Wei, *ACS Nano* **2009**, *3*, 2177.

[41] V. Subramanian, H. W. Zhu, B. Q. Wei, *Electrochem. Commun.* **2006**, *8*, 827.

[42] X. Li, B. Q. Wei, *Nano Energy* **2012**, *1*, 479.

[43] S. Ahmadi, C. H. Chia, S. Zakaria, K. Saeedfar, N. Asim, *J. Magn. Magn. Mater.* **2012**, *324*, 4147.